CHAPTER 3

DESIGN, ANALYSIS AND BEAM-WAVE INTERACTION STUDIES OF FIXED FREQUENCY (95 GHZ 100kW CW, $TE_{6,2}$ MODE) GYROTRON OPERATED IN THE WHISPERING GALLERY MODE

3.7. Conclusions

3.1. Introduction

As discussed in the Chapter 1, gyrotron oscillators are potential RF sources in several applications based on its power level and spectrum of generated frequencies. In the present work, we aimed to study the design of the medium power level gyrotrons used for security applications in the W band regime. As a part, we have selected the design goals of an RF source that able to generates an RF power of more than 100kW power, with efficiency >35% at 95GHz frequency, the beam parameters are taken from the a datasheet of the CPI gyrotron labelled with **VGB8095** so in the rest of the work, it is referred by [VGB8095].

In the literature, various gyrotrons of 100kW, 95 GHz operated in $TE_{6,2}$-, $TE_{7,3}$- and $TE_{10,4}$- are reported [VGB8095, Kumar *et al.* (2013), and Krishna *et al.* (2011)]. Out of which, TE_{62}- based gyrotrons have designed and tested experimentally reported by CPI, $TE_{7,3}$- mode based gyrotron has been reported by [Kumar *et al.* (2013)] and the initial studies mode selection of $TE_{10,4}$- operated device has been reported by [Krishna *et al.* (2011)] whereas the complete design studies that includes the beam wave interaction RF behaviour and thermal studies and the post RF interaction cavity component design are not presented.

As a first step towards our present research work in the field of gyrotron oscillators, considering the operating specifications and design goals of 95 GHz, 100 kW, $TE_{6,2}$ mode gyrotron by Communication and Power industries [VGB8095], the RF interaction cavity design, analysis and the beam wave interaction mechanisms are studied using the linear and non-linear theories reported in the literature. In addition, 3D PIC simulations for the beam present conditions are performed reconfiguring a commercial code "CST studio suite". Later, considering practical values of the electron

beam velocity spreads, the design is investigated for the various beam parameters. Also, the effect of misalignments condition in the beam source on the gyrotron performance is studied. After an intensive RF study of the gyrotron interaction structure, the thermal effects due to the RF power generation in the RF interaction cavity are explored. Design of the required thermal system and its needed suitable optimization to achieve the desired performance of the RF interaction structure is presented. We have further explored and validated our thermal system design using a commercial PIC tool, which is so far not reported in the published literature approachable to the authors. We have used commercial tool "COMSOL Multiphysics" for this purpose and analysed the designed, optimized cooling system for the gyrotron.

The present chapter, Chapter 3 is organized as follows. A brief introduction about various design constraints and the limiting factors required of the gyrotron design are presented. Then by the cavity design using linear theory along with study of beam wave interaction mechanisms under various modes in gyrotrons using precise theory of nonlinear, time dependent, multimode analysis developed by [Fliflet *et al.* (1991)] are presented. Then, the gyrotron RF interaction structure (tapered cylindrical cavity) model is simulated in the commercial CST Studio suite environment, using PIC simulation code the beam wave interaction mechanisms are also investigated. Followed by the thermo-mechanical studies that are essential due to the ohmic losses which leads deformations in the cavity thus degradation of device performance is studied. Using the commercial COMSOL Multiphysics, the optimized cooling system design for the present gyrotron is investigated in depth.

3.2. Design constraints and operating mode selection of Gyrotron

As we know, for any device design, it has to obey certain design requirements as well constraints. Similarly, for the gyrotron oscillators, it has to obey parameters, like, voltage depression (V_{dep}), limiting current (I_L), ohmic losses (dP/dA), fresnel parameter (C_F), etc. Gyrotrons operates at near cut-off frequency of the RF interaction cavity and radiate desired power at the targeted frequencies in $TE_{m,p}$ modes where m and p represents number of full wave and half wave variations in the azimuthal and radial directions. Based on the values of m and p values, in gyrotrons, the modes are classified as axisymmetric modes (m = 0), whispering gallery modes (where $m >> n$, p = 1, 2), volumetric modes (where $m >> n$, $p > 2$) [Edgcombe (1993), and Kartikeyan *et al.* (2013)].

Based on the operating mode and frequency of operation, the probable interaction cavity radius R_c and electron beam radius R_b are given by [Nusinovich (2004)]:

$$R_c = \frac{\chi_{mp}\lambda}{2\pi} = \frac{\chi_{mp}c}{2\pi f_c} \text{ and } R_b = \frac{\chi_{m\pm s,i}R_c}{\chi_{mp}} = \frac{\chi_{m\pm s,i}\lambda}{2\pi} = \frac{\chi_{m\pm s,i}c}{2\pi f_c} \tag{3.1}$$

where χ_{mp} is the p^{th} root of m^{th} order Bessel function of the first kind $J'_m(x) = 0$, c is the velocity of light in free space, f_c is the frequency of operation and where s is the harmonic number and i indicates the number maximum position of the field where the beam is to be launched in the interaction structure. The above stated relations give a probable radius values and sometimes needs a mild variations for optimized performance of the design.

Selection of suitable operating mode followed by optimization of interaction cavity dimension and beam parameter for achieving the design goal is two major steps

for the device design. The design goal and technical constraints of the present design are tabulated in the following Table 3.1.

Table 3.1: Design goal and technical constraint values

Parameter	Value
Frequency f	95±0.1 GHz
Output power P_{out}	> 100 kW
Diffractive quality factor Q_{diff}	800-900
Beam current	5 A
Beam voltage V_b	50 kV
Magnetic field at the cavity B	3.60±0.3 T
Pitch factor α	1.4-1.5
Harmonic number, s	1
Interaction efficiency η	>35%
Wall losses dP_{loss}/dA	< 2 kw/cm^2

Gyro-devices have to satisfy the design constraints while reaching the targeted goal for longer life as well reliable operation. Likewise, gyrotron oscillator has to obey design constraints under a limit like voltage depression V_{dep}, limiting current I_L, ohmic losses dP_{loss}/dA, along with significant frequency separation of operating mode from the competing modes [Edgcombe (1993), and Kartikeyan *et al.* (2013)]. In the following sub-sections, a brief description of the major design constraints and its role on the gyrotrons performance are presented.

3.2.1. Voltage Depression (V_{dep})

Owing to the space charge in the beam, the potential within the beam is reduced with respect to the wall potential. This phenomenon is called the voltage depression. The depression in the potential produces spread in the electron beam causes poor beam quality as well as reduction in efficiency. Lower values of voltage depression V_{dep} is

always desirable and in the cylindrical interaction cavity of gyrotrons, it is given by [Edgcombe (1993), and Kartikeyan *et al*. (2013)].

$$V_{dep} \approx 60 \frac{I_b}{\beta_z} \ln\left(R_c / R_b\right), \tag{3.2}$$

where R_c , R_b ,I_b, β_z are the interaction cavity radius, beam radius, beam current, normalized axial velocity of electrons, respectively.

3.2.2. Limiting Current (I_L)

The limiting current I_L is defined as the current beyond which the voltage depression becomes so large that the axial beam velocity tends to zero and the beam no longer propagates but is reflected [Edgcombe (1993), and Kartikeyan *et al*. (2013)]. The limiting current I_L can be given by:

$$I_L = \frac{2\pi\varepsilon_0 m_e c^3}{q_e}\left[\frac{\gamma_0\left(1-\left(1-\beta_{z0}^2\right)^{1/3}\right)^{3/2}}{\ln\left(R_c / R_b\right)}\right] \text{ where } \gamma_0 = 1 + \frac{q_e V_b}{m_e c^2} \ . \tag{3.3}$$

Here V_b is the beam voltage, q_e is the charge of the electron, m_e is the mass of the electron, γ_0 is the Lorentz factor or relativistic mass factor of the electron. Generally limiting current should be at least twice as large as the operating current of the device.

3.2.3. Ohmic Wall losses (dP_{loss}/dA)

The finite conductive nature of the interaction cavity walls of the device results losses in the cavity region in terms of ohmic losses. These losses are related by amount of targeted power P_{out}, quality factor Q_{diff}, operating mode and the dimensions of the structure. Ohmic losses plays critical role in the stable operation of the device due to thermo-mechanical dependency of the cavity materials that causes deviations in the RF

behaviour. The peak of the ohmic losses in the gyrotron oscillator can be given as [Edgcombe (1993), and Kartikeyan *et al.* (2013)]:

$$\left(\frac{dP_{loss}}{dA}\right)_{\max} \approx \sqrt{\frac{1}{30\sigma}}\left[\frac{f^{3/2}P_{out}Q_{diff}}{c^{3/2}L_c}\right]\left[\frac{1}{\chi_{mp}^2 - m^2}\right] \tag{3.4}$$

where Z_0 = 377 Ω is the intrinsic impedance for the vacuum, effective length of the interaction cavity L_c, σ is electrical conductivity of the cavity material. It is a limiting factor and generally should be kept below 2 KW/cm^2 for high power devices. Lower ohmic losses are desirable for stable frequency of operation and longer device life, and yields simple, efficient thermal management system design.

Since gyrotron operates in the high order mode that leads to presence of dense mode spectrum, hence, in addition to the above design constraints, knowledge of the frequency separations between the main operating mode and the competing modes also becomes important. The frequency of separation should be as wide as possible to avoid mode competition. For a TE$_{m,p}$ mode, the most competing modes are TE$_{(m-1),p}$ and TE$_{(m-3),(p+1)}$ and theoretically the frequency separation from these modes are determined by [Kumar *et al.* (2014)]:

$$\Delta f_1(\%) = \frac{\chi_{m,p} - \chi_{m-1,p}}{\chi_{m,p}} \times 100 \; and \; \Delta f_2(\%) = \frac{\chi_{m,p} - \chi_{m-3,p+1}}{\chi_{m,p}} \times 100 \tag{3.5}$$

Considering the design constraints and requirements of the device, a suitable operating mode selection is required for the achievement of the targeted goals. Sometimes, it is not feasible for modes to maintain all the design constraint within the limits and a trade-off among constraints needs to be considered. In the present chapter,

we have taken the operating mode and beam parameters from the CPI-VGB 8095, so no need of mentioning a detailed procedure to choose the operating mode. Hence, we moved with design, analysis and simulation of the RF structure that is able to meet the targeted goals. Considering several compete modes, the design constraints have been calculated for the beam parameters listed in Table 3.2. Considering effective length of the interaction cavity as 20 mm, at the design parameters listed in Table 3.1, using expressions 3.1-3.5, the design constraints for various modes are calculated and tabulated in the Table 3.2.

Table 3.2: Design constraints values for different modes

m	**n**	X_{mp}	R_c **(mm)**	R_b **(mm)**	V_d **(kV)**	I_L **(A)**	dP/dA_{max} **(kW/cm^2)**	m/X_{mp}	Δf_1	Δf_2
1	4	11.7048	5.8828	1.9256	1.4059	22.443	0.1639	0.0854	13.8210	39.653
1	4*	11.7048	5.8828	1.5348	1.6915	18.654	0.1639	0.0854	13.8210	39.653
2	4	13.1692	6.6187	0.9252	2.4771	12.738	0.1316	0.1518	11.1193	12.856
2	4*	13.1692	6.6187	2.1113	1.4385	21.9358	0.1316	0.1518	11.1193	12.856
3	3	11.345	5.7019	1.5348	1.6522	19.098	0.1862	0.2644	12.1323	17.431
3	3*	11.345	5.7019	2.6723	0.9541	33.072	0.1862	0.2644	12.1323	17.431
4	2	9.28171	4.6649	2.1113	0.9980	31.615	0.3179	0.4309	13.6517	8.0398
4	2*	9.28171	4.6649	3.2242	0.4650	67.854	0.3179	0.4309	13.6517	8.0398
4	3	12.6809	6.3733	2.1113	1.3909	22.686	0.1540	0.3154	10.5350	7.6970
4	3*	12.6809	6.3733	3.2242	0.8579	36.781	0.1540	0.3154	10.5350	7.6970
5	2	10.5191	5.2868	2.6723	0.8589	36.736	0.2603	0.4753	11.7635	5.2338
5	2*	10.5191	5.2868	3.7698	0.4257	74.112	0.2603	0.4753	11.7635	5.2338
6	**2**	**11.7341**	**5.8975**	**3.2242**	**0.7602**	**41.5076**	**0.2193**	**0.5113**	**10.3546**	**3.3165**
6	2*	11.7341	5.8975	4.3109	0.3945	79.978	0.2193	0.5113	10.3546	3.3165
6	3	15.2671	7.6731	3.2242	1.0915	28.907	0.1131	0.39300	8.3902	4.4703
6	3*	15.2671	7.6731	4.3109	0.7259	43.4698	0.1131	0.3930	8.3902	4.4703
10	1	11.7702	5.9156	5.3832	0.1187	265.737	0.5786	0.8496	9.0006	9.8668
10	1*	11.7702	5.9156	6.4461	0.1081	291.82	0.5786	0.8496	9.0006	9.8668

Inspecting the design constraints of various mode, it is found that $TE_{6,2}$ is possessing desired qualities at the given parameter. The limiting current I_L and voltage depression V_{dep} curves for the $TE_{6,2}$- mode over a range of normalized beam radius values are calculated for beam parameters listed in Table 3.1 and plotted in Figure 3.1

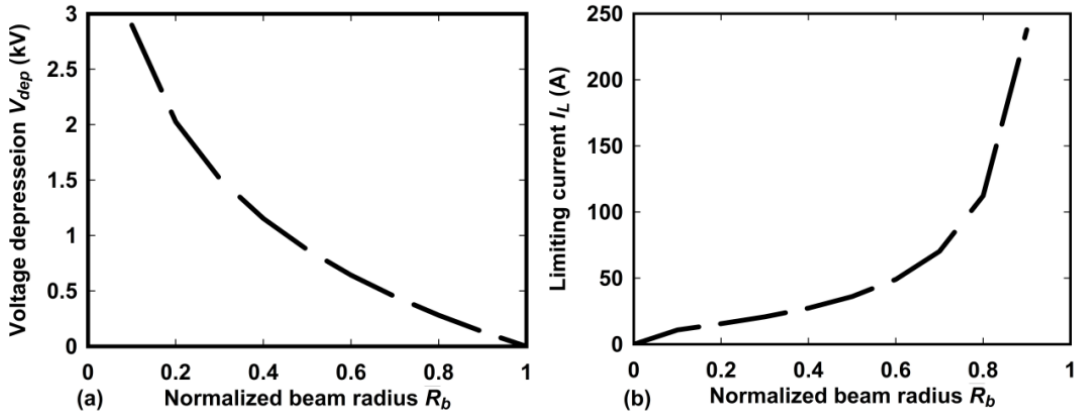

Figure 3.1: (a) Voltage depression V_{dep} (kV) versus normalized beam radius $\overline{R_b}(=R_b/R_c)$, and (b) Limiting current I_L (A) versus normalized beam radius $\overline{R_b}(=R_b/R_c)$ for $TE_{6,2}$- mode.

The RF interaction cavity that provides space for the beam wave interaction is to be designed. The role of the interaction structure is to allow the growth of the operating mode at desired frequency of oscillation while suppressing the mode conversion when subjected to the beam parameters. The background analysis required for the RF cavity design and the selection of the cavity dimensions are presented in the following subsection.

3.3. Design of RF Interaction structure

A conventional tapered cylindrical structure as RF interaction cavity is taken in the present design and its 2-D axis symmetric model view is shown in Figure 3.2. It consists of three sections, first a down taper section for RF isolation of length L_d, with an angle θ_d, followed by a uniform middle section where active beam-wave interaction

takes place, of length L_c and at the end, an up-taper section where RF standing waves get converted into travelling waves to extract out RF energy, of length L_u with angle θ_{up}. Usually, parabolic smoothing section of lengths L_{ds} and L_{us} at down-taper and up-taper transitions, respectively, are used to minimize the mode conversions [Edgcombe (1993), Kartikeyan *et al.* (2013)].

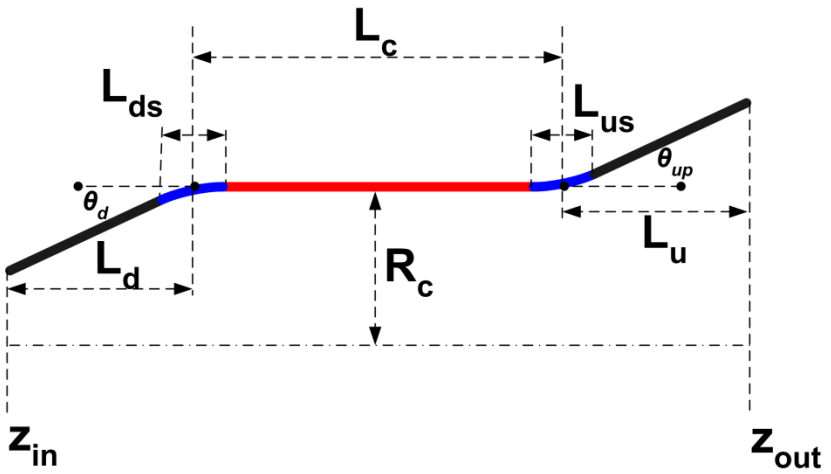

Figure 3.2: 2-D axis symmetric view of the tapered RF interaction cavity of the gyrotron.

Design of interaction cavity requires knowledge of axial RF field profile $V_{mp}(z)$, resonating frequencies f_{res}, and its quality factor Q_{diff}. If the taper angles are small (< 10^0), it is appropriate to use the single mode Vlasov approximation in which only single $TE_{m,p}$ mode is retained in the expansion of coupled equations and coupling due to the other modes due to cavity tapers can be neglected. Thus, in single mode approximation, the RF field profile $V_{mp}(z)$ in the interaction structure can be given by [Edgcombe (1993)]:

$$\frac{d^2V_{mp}}{dz^2}+\left(\frac{\omega^2}{c^2}-k_{mp}^2(z)\right)V_{mp}\simeq+i\omega J_{mp}, \tag{3.6}$$

where $J_{mp} = \int d\phi \int_0^{R_c} \mathrm{Re}^*_{mp} . J dR.$ is the source term, the complex RF frequency $\omega = \omega_{res}\left(1 + i/2Q_{diff}\right)$, ω_{res} resonant frequency and the transverse wave number $k_{mp}(z) = \chi_{mp} / R(z).$ The functions $V_{mp}(z)$ must satisfy radiation boundary conditions at the ends of the interaction cavity and can be written as:

$$\left.\frac{dV_{mp}}{dz}\right|_{z_{in}} = ik_z(z_{in})V_{mp}(z_{in}),\ and\ \left.\frac{dV_{mp}}{dz}\right|_{z_{out}} = -ik_z(z_{out})V_{mp}(z_{out}). \tag{3.7}$$

Here, k_z is the axial wave number and given by $k_z(z) = \sqrt{(\omega/c)^2 - k_{mp}^2(z)}$, z_{in} and z_{out} are the down taper and up taper axial ends of the interaction structure. The solution of expression (3.6) using the boundary conditions (3.7) is best carried out with the Numerov algorithm when the source term is set as: J_{mp}=0 [Numerov (1927)]. With a systematic cavity design procedure calculations are performed for various cavity geometry combinations. The suitable combinations and the corresponding cavity parameters in the cold condition (beam absent) i.e., J_{mp}= 0 are tabulated in Table 3.3.

Table 3.3: RF cavity parameter for various cavity combinations

Parameter	**Set#1**	**Set#2**	**Set#3**
L_d (mm)	13	13	13
L_c (mm)	20	20	20
L_{up}(mm)	23	23	23
θ_d	2.2^0	2.2^0	2.2^0
θ_{up}	2.8^0	2.8^0	2.8^0
L_{ds} (mm)	0	4	6
L_{us}(mm)	0	4	6
f_{res}(GHz)	95.004	95.01	95.033
Q_{diff}	1110	924	735

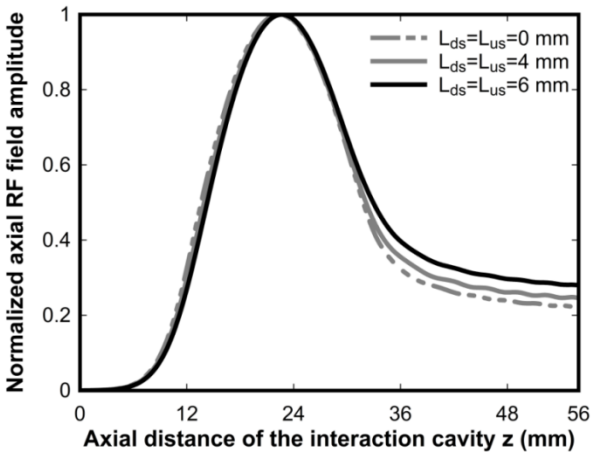

Figure 3.3: Normalized axial RF field amplitude profiles for various smoothing transition combinations at 0 mm, 4 mm, 6mm of lengths: L_d = 13 mm, L_c = 20 mm and L_{up} = 26 mm.

The normalized axial RF field amplitude profiles for various parabolic smoothing transition combinations for fixed cavity lengths (L_d, L_c *and* L_{up}) are plotted in Figure 3.3. It is observed that for increasing smoothing transitions, leads lower diffractive quality factor along with slight rise of reflection in the up taper region.

Table 3.4: Optimized tapered RF cavity dimensions

Parameter	**Value**
Cavity radius R_c	5.90 mm
Down taper length L_d	13 mm
Middle section Length L_c	20 mm
Up taper length L_u	23 mm
Parabolic smoothing L_{ds}	4 mm
Parabolic Smoothing L_{us}	4 mm
Down taper angle θ_d	2.2^0
Up Taper angle θ_{up}	2.8^0
Resonant Frequency f_{res}	95.01 GHz
Diffractive quality factor Q_{diff}	924

Following the determination of probable RF cavity dimensions, the designed beam parameters need to be optimized such that accomplishment of desired operation

with the minimum mode competition is achieved. The optimum radius and possible operating modes are determined by the calculations of the beam coupling coefficient as well the start oscillations currents of the several modes. A brief theory and its calculations for the current design are presented below.

3.3.1. Coupling Coefficient (C_{mp})

The optimum beam radius that results high beam wave coupling is estimated by coupling coefficient C_{mp} curves and can be obtained using the following expression [Edgcombe (1993), and Kartikeyan *et al.* (2013)]:

$$C_{mp}^2 = \frac{J_{m\pm s}^2\left(\chi_{mp} R_b / R_c\right)}{\left(\chi_{mp}^2 - m^2\right) J_m^2\left(\chi_{mp}\right)} \tag{3.8}$$

These curves are mode dependent and provide the amount of beam wave coupling value with respect to normalized beam radius for the uniform cavity radius R_c. The optimum beam radius is taken, such that, achieving maximum coupling and have significant distance away from both the walls as well axis of the structure. Considering various modes, the coupling coefficient C_{mp} curves for various modes with respect to normalized beam radius $\overline{R_b} = R_b / R_c$ are shown in Figure 3.4. It can be observed that the maximum coupling for the desired mode $TE_{6,2}$- occurs at normalized beam radius $\overline{R_b}$ = 0.545, accordingly electron beam radius is selected as 3.224 mm. It can be observed that the coupling coefficient for $TE_{3,3}$- mode is high compared to operating mode, but its stays to far from the cavity.

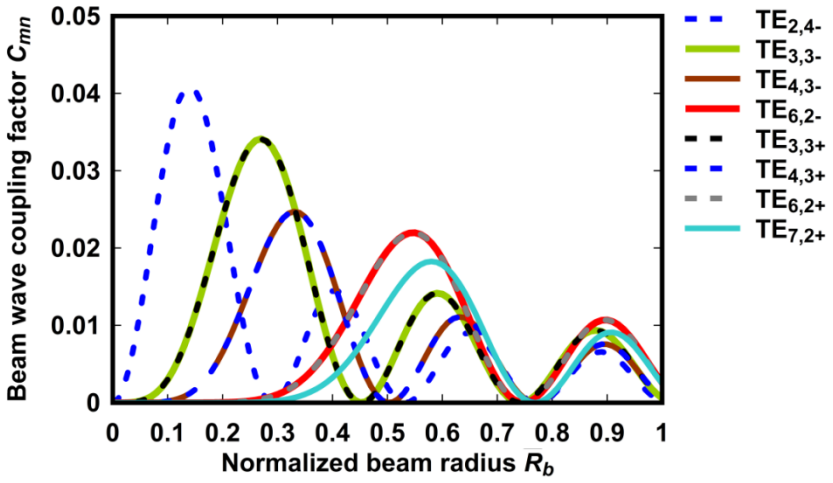

Figure 3.4: Beam wave coupling factor C_{mp} curves versus normalized beam radius($\overline{R_b}$) for various modes

3.3.2. Start Oscillation Current (I_{soc})

Though, the present design is for $TE_{6,2-}$, it is very important to determine the nearby and compete modes that can resists the mode growing. In high order operating mode devices, the competition from the nearby modes is inevitable and draws significant power from the electron beam causes power loss as well as reduction in device efficiency. Hence, identification of the competing modes is necessary and determined by the start oscillation current I_{soc} curves. It is defined as the minimum amount of current that allows the mode to oscillate significant and starts growing. The start oscillation current I_{soc} are calculated using linearized single-mode gyrotron theory and can be given as [Edgcombe (1993), and Kartikeyan *et al.* (2013)]:

$$I_{start}(\Delta,\mu) = 8.56x10^4 \frac{\exp\left((\mu\Delta)^2/8\right)}{\mu^2\left(\mu^2\Delta - 4s\right)} \frac{L_c\gamma_0}{Q\lambda}\left(\frac{\beta_{t0}^{2(3-s)}}{C_{mp}^2}\right) \tag{3.9}$$

where C_{mp} is the coupling coefficient and given by expression (3.9), and μ is normalized length of the interaction cavity, Δ is frequency mismatch or detuning parameter which are defined as [Edgcombe (1993), and Kartikeyan *et al.* (2013)]:

$$\mu = \frac{\pi \beta_{t0}^2 L_c}{\beta_{z0} \lambda} \; and \; \Delta = \frac{2}{\beta_{t0}^2}\left(1 - \frac{s\omega_{c0}}{\omega}\right) \quad . \tag{3.10}$$

Here, s is the harmonic number, β_{t0} is the normalized transverse velocity at the entrance of the interaction region, ω_{c0} is the non-relativistic cyclotron frequency [Kartikeyan *et al.* (2013)]. Considering the beam parameter as mentioned in Table 3.1 and for the cavity parameter as per Table 3.2, by varying the background DC magnetic field from 3.4 T to 3.7T, the start oscillation current I_{soc} values for various modes are calculated and plotted in Figure 3.5. In the I_{soc} calculation we considered the modes whose Eigen values are in the range of difference 3 from the desired mode Eigen value, i. e., $\chi_{mp} \pm 3$.

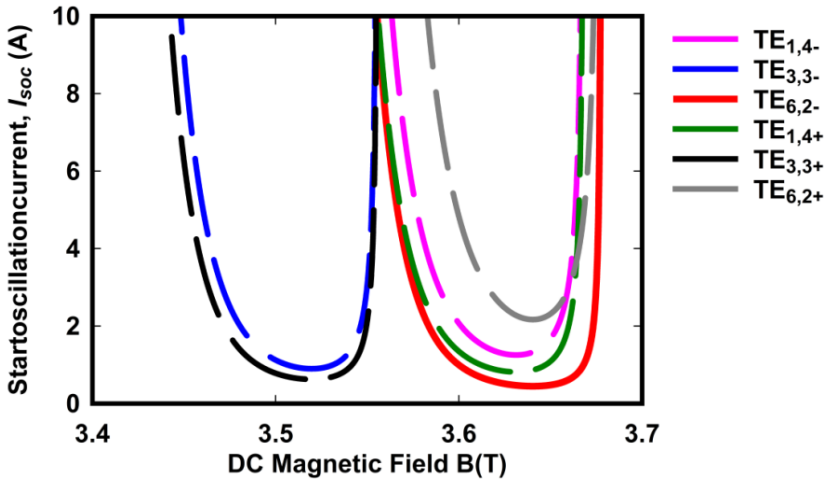

Figure 3.5: Start oscillation current Isoc (A) versus DC magnetic field B in (T) plots for different operating modes.

From the start oscillation current I_{soc} curves, it can be observed that $TE_{3,3+}$ and $TE_{1,4+}$ are some potential competing modes, however a suitable selection of DC magnetic field can reduce its significance. The role and significance of compete modes at various beam parameters in the beam wave interaction analysis and simulation are discussed in the following sections.

3.4. Beam-wave interaction study

Taking the probable set of beam parameters and cavity dimension as obtained from Section 3.2, by studying the electron beam and RF wave interaction mechanism for operating mode along with competing modes, the design is to be confirmed with the optimized parameters. In the present section the beam wave interaction mechanism is studied analytically using time dependent multimode analysis as well as the interaction cavity is simulated using commercial CST studio suite. The time dependent theory and the procedure for simulations in the CST studio suite environment is described in the coming sections.

3.4.1. Time-Dependent Multimode Theory

A self-consistent time-dependent multimode nonlinear analysis developed by Fliflet *et al.* (1991) is widely accepted for the study of the electron-beam and RF-wave interaction mechanism in the gyro devices. This theory is implemented in our work to study beam wave interaction behaviour of the gyrotron device. Space charge effects are neglected. A brief theory about the various set of coupled differential equations that governs the calculations of electron trajectories in the interaction structure as well the temporal behaviour of several modes are presented below.

In a highly overmoded gyrotron cavities, the mode spectrum is very dense and electron is likely to interact several modes in the cavities which leads to unstable the device and lower the efficiencies. Hence, for a high efficiency gyrotron, it is a challenging task to avoid the mode competition. Mode interaction theory has been presented by many of authors in the past [Bondeson *et al.* (1983), Kreischer *et al.* (1984)]. However, the single mode operation is indeed possible if the design of interaction structure is appropriate and the start oscillation current criteria are properly

analysed for the designed cavity. To study the performance of the overmoded cavities in the presence of several nodes, a multimode theory is presented here based on the formulation done by [Fliflet *et al.* (1991)].

In the analysis, a thin gyrating beam of electrons is considered. The arrangement of gyrating electron beam in a cylindrical cavity with all its coordinates is shown in Figure 3.6. Electrons move on a helical path gyrating about the guiding centre radius r_b. It is considered that electron beam interacts with the one or more competing modes closely spaced in the cavity.

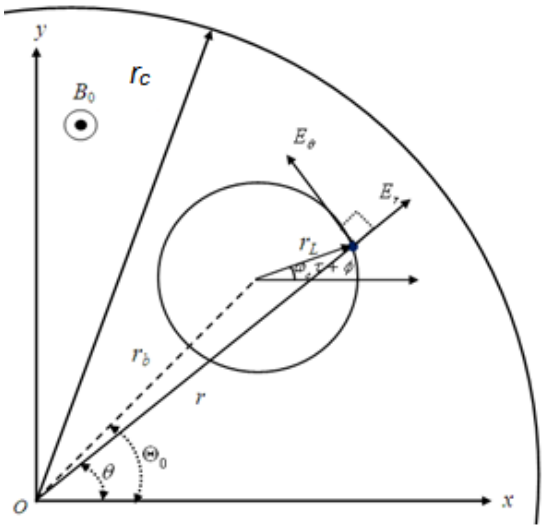

Figure 3.6: Arrangement of the gyrating electrons in Larmor orbit in the Cartesian as well as cylindrical coordinate systems.

The Lorentz's force equation governing motion of electrons in the presence of perturbing RF fields is given by

$$\frac{dP}{dt} + \frac{|e|}{\gamma m_e} P \times B_0 = -|e|(E + \frac{1}{\gamma m_e} P \times B) \equiv a' \quad , \qquad (3.11)$$

where, B_0 is the applied magnetic field $(B_0 = B_0\hat{z})$, P is the momentum of the electron, E and B are the electric and magnetic fields, and γ is the relativistic mass factor defined as $\gamma = [1 + p^2/(m_e c)^2]^{1/2}$.

Electrons interaction with RF fields result in perturbations in their momentum and phase, i. e., their momentum and phase deviate from the normal values they would have possessed if there were no interaction. To facilitate tracking of changes in the momentum and phase of electrons and with an observation on the most suitable co-ordinate system, the cylindrical co-ordinate system in this context is considered. Hence, the representing transverse momentum can be written in the form

$$p_x + ip_y = ip_t \exp[i(\omega_c \tau + \varphi)] \quad , \tag{3.12}$$

where, p_t and φ are slow time scale magnitude and phase of transverse momentum. The term slow time scale indicates those temporal derivatives of the two, momentum and phase, are quiet less than operating frequency (ω_0) or the reference cyclotron frequency (ω_c). Before interaction, the above equation (3.12) can be written as

$$p_x + ip_y = ip_t \exp[i(\omega_c \tau + \varphi_0)] \ , \tag{3.13}$$

where φ_0 and p_t are constants, the initial gyro-phase of an electron in a beam let and $\left[p_x^2 + p_y^2\right]^{1/2}$, respectively.

Hence, finally one can get the expressions for the momentum and phase of the particles [Fliflet *et al.* (1991)] as,

$$\frac{dp_t}{d\bar{z}} = \frac{\gamma}{p_z} \sum_{n=1}^{N} f_n J_s'\left(\bar{k}_{nt}\bar{r}_L\right) \mathrm{Re}\left\{\left[h + i\frac{p_z}{\gamma\omega_0}\frac{dh}{d\bar{z}}\right] e^{-i\left(\Lambda + \bar{\psi}_n + (m_n - s)\Theta_0\right)}\right\} \tag{3.14}$$

$$\frac{d\Lambda}{d\bar{z}} = \varpi_0\left[1-\frac{s\varpi_c}{\varpi_0\gamma}\right] - \frac{s\gamma}{p_z p_t}\sum_{n=1}^{N} f_n \frac{J_s^{'}\left(\bar{k}_{nt}\bar{r}_L\right)}{\bar{k}_{nt}\bar{r}_L}\mathrm{Re}\left\{\left[h + i\frac{p_z}{\gamma\bar{\omega}_0}\frac{dh}{d\bar{z}} - \frac{\varpi_{n0}^2 p_t^2}{s\varpi_c\varpi_0\gamma}h\right]e^{-i\left(\Lambda+\bar{\psi}_n+\left(m_n-s\right)\Theta_0\right)}\right\} \tag{3.15}$$

$$\frac{dp_z}{d\bar{z}} = \frac{p_t}{p_z\varpi_0}\sum_{n=1}^{N} fnJ_s^{'}\left(\bar{k}_{nt}\bar{r}_L\right)\mathrm{Re}\left[i\frac{dh}{d\bar{z}}e^{-i\left(\Lambda+\bar{\psi}_n+\left(m_n-s\right)\Theta_0\right)}\right] \quad , \tag{3.16}$$

where, γ is updated as

. The linearized mode phase parameter can be given as $\bar{\psi}_n(z) = \psi_n(t_0) + \left.\frac{d\psi_n}{dt}\right|_{t_0} z/v_z$.

Variables with bar are the normalized and are given as $\bar{r}_L = \frac{r_L}{r_{co}}, \overline{\omega_c} = \frac{\omega r_{co}}{c}, \bar{k}_{nt} = k_{nt}r_{co}, \bar{z} = \frac{z}{r_{co}}, \bar{\omega}_0 = \frac{\omega r_{co}}{c}$, and the slow time variations of azimuthal momentum phase with respect to the reference wave is given by, $\Lambda = (\omega_0 - s\omega_c)\tau + \omega_0 t_0 - s\varphi - (m_n - s)\theta_0$.

The normalized RF field amplitude and phase can be obtained from (3.17) and (3.18) as [Fliflet *et al.* (1991)] :

$$\frac{df_n}{d\tau} = -\frac{f_n}{2Q_n} + \bar{I}_n\int_0^L d\bar{z}h(\bar{z})\left\langle J_s^{'}\left(k_{nt}\bar{r}_L\right)\frac{p_t}{p_z}\cos\left(\Lambda+\bar{\psi}_n+\left(m_n-s\right)\Theta_0\right)\right\rangle_{\Lambda_0,\Theta_0} \tag{3.17}$$

$$\frac{d\Psi_n}{d\tau} = -\frac{\omega_0-\omega_{n0}}{2Q_n} - \frac{\bar{I}_n}{f_n}\int_0^L d\bar{z}h(\bar{z})\left\langle J_s^{'}\left(k_{nt}\bar{r}_L\right)\frac{p_t}{p_z}\sin\left(\Lambda+\bar{\psi}_n+\left(m_n-s\right)\Theta_0\right)\right\rangle_{\Lambda_0,\Theta_0} \tag{3.18}$$

where f_n and I_n are given by equation (3.19) and (3.20).

$$f_n = \frac{|e|}{m_e c^2}x_n^{'}C_n J_{m_n-s}\left(k_{nt}r_b\right)a_n\left(t_0\right), \tag{3.19}$$

$$I_n = \frac{|e|Z_0}{m_e c^2 \overline{\omega_o}} \frac{J^2_{m_{n-s}}\left(k_{nt} r_b\right)}{\pi\left(1-\frac{m_n^2}{x'^2_{m_n l_n}}\right) J^2_{m_n}\left(x'^2_{m_n l_n}\right)\overline{W}} I_0 \tag{3.20}$$

For co-rotating modes, $m_n > 0$, and for counter rotating modes, $m_n < 0$. Therefore, the time-dependent output power in the mode n can be obtained as,

$$P_n(\tau) = \frac{\pi m_0 c^4}{2Z_0|e|^2} \frac{\left(1-m_n^2/x'^2_{m_n l_n}\right) J^2_{m_n}\left(x'_{m_n l_n}\right)}{J^2_{m_{n-s}}\left(k_{nt} R_0\right)} \varpi_0 \overline{W} \left| f_n(\tau) \right|^2, \tag{3.21}$$

and the total interaction efficiency can be obtained by the energy distribution of all the particles as

$$\eta = \frac{\gamma_0 - \left\langle \gamma(z=L) \right\rangle_{\Delta_0,\Theta_0}}{\gamma_0 - 1} \quad , \tag{3.22}$$

where, $\langle \quad \rangle_{\Delta_0,\Theta_0}$ denotes the average over all the initial phase of all the particles.

3.4.2. Computational results and discussion

Using this multimode theory, the beam-wave interaction behaviour in the interaction cavity region, considering several modes can be studied on the time basis. The calculation is starts by assigning a small amplitudes and random phases to a set of modes. Then, solving the coupled, nonlinear, differential equations describing the electron momentum and phase equations along with the coupled time-dependent equations describing the mode amplitude and phase equations at each time step, the time varying behaviour of various modes are determined. Consequently, with the help of mode amplitudes and phases, the temporal growth of power levels in the modes and the electronic efficiency are calculated.

In the present study, considering a uniform background DC magnetic field profile along the interaction length, the coupled equations are numerically integrated using fourth order Runge-Kutta method. Considering a ramp type of DC beam voltage source from 35 kV to 50 kV with a period of rise time 200 ns is taken and a 5amps of DC currents is assigned to an electron beam that are generated with a pitch factor 1.414. The generated electron beam is injected into interaction region and is guided by external uniform DC magnetic field. In the calculation, the electrons are uniformly distributed gyrating with 32 beamlets with 32 electrons in each beamlets. With the space step size of 0.1 mm (< λ/30) as well a time step size of 5ps, the time dependent multimode analysis are done. For the operating and its neighboring modes, like, $TE_{3,3+}$, $TE_{3,3}$-, $TE_{10,1+}$, $TE_{10,1}$-, $TE_{6,2}$-, and $TE_{6,2+}$ beam-wave interaction behaviour are observed and its temporal power growth P_m are determined versus simulation time and are plotted in the Figure 3.7. Efficiency of the device is shown in Figure 3.8.

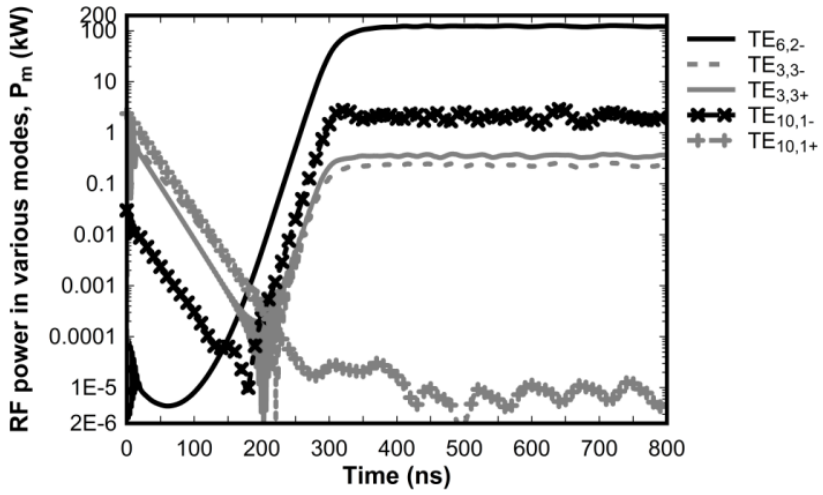

Figure 3.7: Temporal growth of output RF powers P_m (kW) in various modes through time dependent multimode analysis.

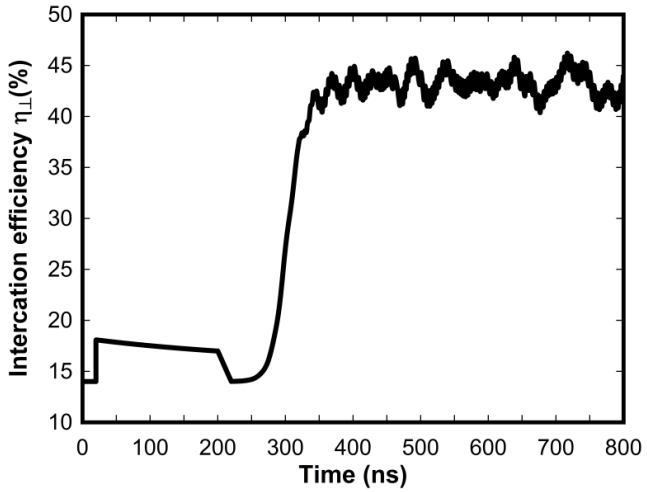

Figure 3.8: Interaction efficiency η versus time (ns).

It can be observed here that initially $TE_{3,3,}$+ mode dominates and after 300 ns it the desired operating mode $TE_{6,2}$- starts growing up to a stable RF power of ~123 kW; while all the competing modes reaches to a minimal value after 320 ns. An electronic efficiency of 40% is achieved at DC magnetic field of 3.60 T. Further, a parametric study is also performed analytically for range of applied DC magnetic fields and is discussed at the end.

3.5. 3D Particle in Cell (PIC) Simulation Studies

Various particles-in-Cell (PIC) codes are available for the study of beam wave interactions in high power microwave sources, like, MAGIC and CST Studio Suite are familiar. Since using MAGIC the beam wave interaction analysis is carried out by assigning a single mode means investigation under more than single mode is not possible. Whereas, using Commercial "CST Studio Suite", the beam wave interaction behaviour of the RF device can be investigated under more than one mode also. Various works [Swati *et al.* (2015), and Singh *et al.* (2013)] are reported in the field of microwave sources that uses CST studio suite for the investigations of beam wave interaction behaviour use in the devices.

In the present work, a 3D Particle in Cell simulation of the electron-beam and RF-wave interaction region of the device is performed reconfiguring a commercial code "CST Studio Suite." In the present study, taking OFHC copper as the cavity material with conductivity of 5.8×10^7 S/m, the RF interaction structure of the device is modeled. A particle circular source is taken for forming the gyrating electron beam with designed beam parameters with rise time of 1ns, that allows to run the simulation for less time than in the analysis, and an external axial magnetic field profile $B(z)$ is applied. To observe the temporal behaviour of modes, various 2D and 3D field monitors are placed with suitable boundary conditions.

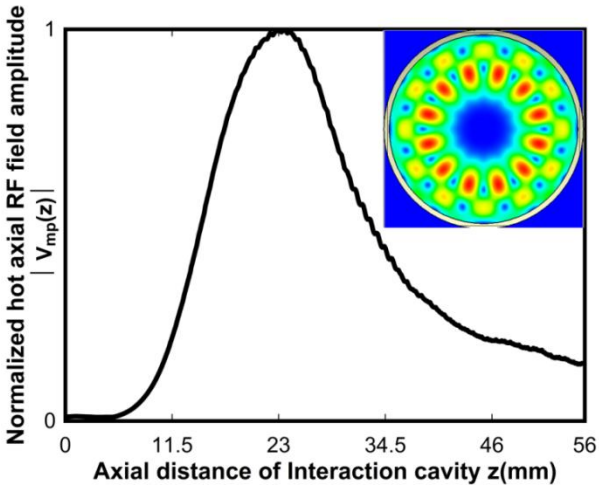

Figure 3.9: PIC simulation results: Normalized axial RF field amplitude profiles hot conditions along with vector field distribution.

3.5.1. Device performance under ideal condition

After the RF interaction cavity design, the desired axial electric field profile and mode excitation inside the cavity in the cold condition (absence of the electron beam) is ensured. Thereafter, by introducing the electron beam, the beam wave interaction behaviour is investigated. The simulated interaction cavity axial RF electric field profile versus axial cavity position in hot (beam present) conditions, and the as vector plot of field pattern of operating mode is shown in Figure 3.9. The time varying field

amplitudes of various modes are monitored using 3D *E*-field monitors and the significant mode amplitudes of the interaction are plotted in Figure 3.10. The operating $TE_{6,2-}$ mode and the main competing modes $TE_{3,3+}$ and $TE_{10,1-}$, at magnetic field B = 3.60T. Here, one can observe that for $TE_{6,2-}$ operating mode RF signal growth stabilizes in 200 ns and competing $TE_{3,3+}$ mode ad $TE_{10,1-}$decay to a minimal value in ~ 210 ns. The '+' and '-' assigned to the modes are confirmed by the orientation of field at particular location in the CST. If the mode rotates in clockwise wise then it is '+' and else it is '-'.

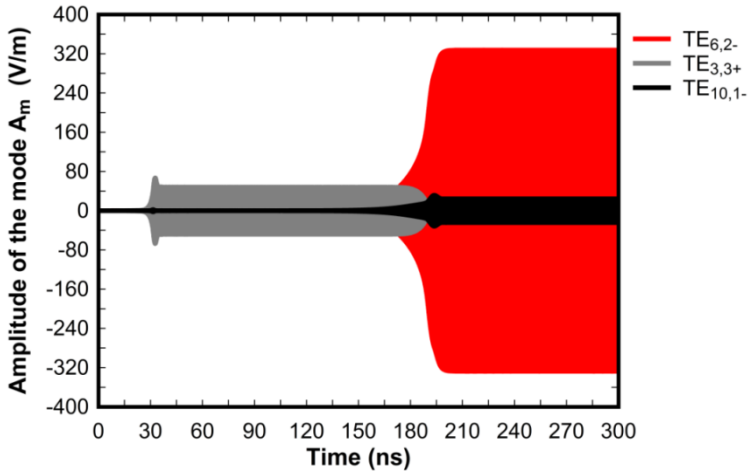

Figure 3.10: Temporal growth of operating and competing mode amplitudes A_m (V/m) from PIC Simulation study.

By post processing the results, the oscillation frequency as well RF power developed across various modes are determined. The temporal power growth is performed for the $TE_{3,3+}$, $TE_{10,1-}$ and $TE_{6,2-}$ modes. The frequency response of the modes is determined by performing Fourier Transform (FFT) action on the mode amplitude signals and the resultant frequency response for the modes are shown in the Figures 3.11 and 3.12. It is observed that the FFT responses of the main mode $TE_{6,2-}$ is at 94.987 GHz . As well from the peaks of the amplitudes of the FFT signals confirms that the $TE_{6,2-}$ is dominant. The temporal power growth in the gyrotron device for $TE_{3,3+}$ and

$TE_{6,2}$- modes are shown in Figure 3.12, where one can readily observe that power transfer from the electron-beam to the RF-wave in different modes with time during device operation.

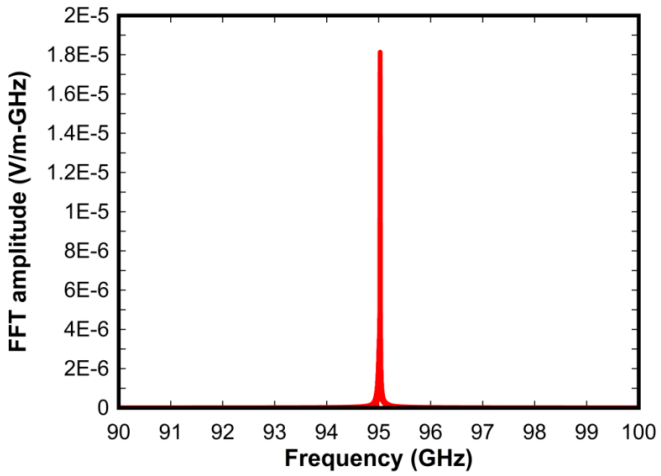

Figure 3.11: Frequency response of the operating and competing modes from PIC simulation study.

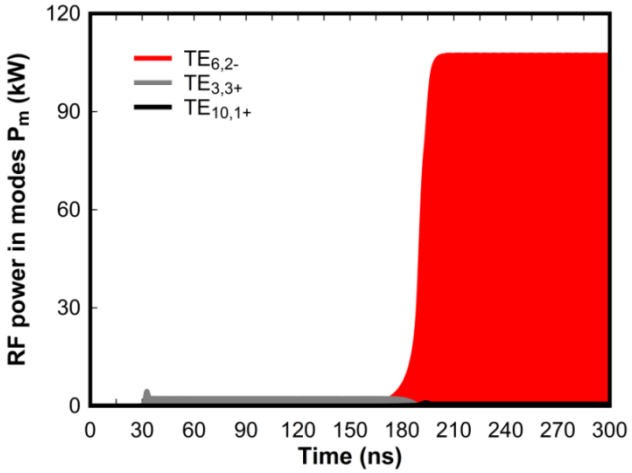

Figure 3.12: CST PIC simulation results- Temporal growth of RF powers in the operating and competing modes.

Around 107 kW stable RF power is generated at oscillation frequency 94.987 GHz in at the desired operating $TE_{6,2}$- mode, while RF power generated in all the competing modes is less than a percent. To strengthen the design study, a parametric analysis of device operation is also carried out for a range of the applied DC magnetic field. The RF output power generated versus applied DC magnetic field is performed

both analytically and also compared for its validation with PIC simulated values as shown in Figure 3.13. As magnetic field increases the RF power levels in the main mode are decreases in both analytical and simulated resulted results. Furthermore, an agreement within 7% is observed between the analytical and PIC simulation results. The discrepancy in the comparisons is because of the consideration of several assumptions in the analysis. Starts with ideal Gaussian type cavity axial E-field profile $h(z)$, zero velocity spreads in the beam and the calculations are limited to uniform section only. Conversely in the PIC simulations, the calculations are performed by including the uptaper section and a practical cavity axial E-field profile $h(z)$ (shown in Figure 3.9).

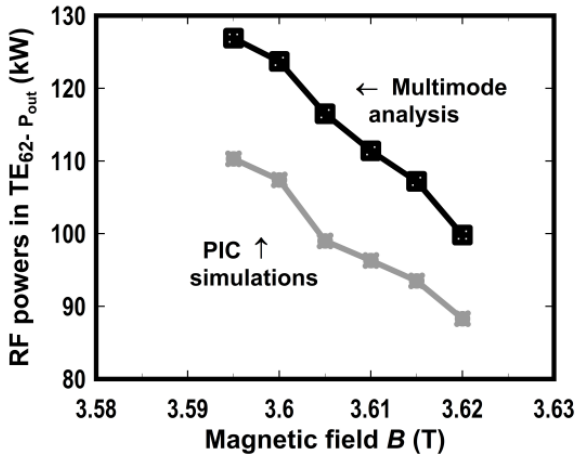

Figure 3.13: Comparisons of output RF powers in the main mode $TE_{6,2}$- by multimode analysis and PIC simulations for magnetic fields .

3.5.2. Device performance under practical conditions

So far, the beam wave interaction studies are carried out by using time dependent multimode theory as well CST studio suite under ideal conditions of beam parameters, i.e., no beam spread in terms of velocity as well beam alignment axis. But, the device performance is often required to be evaluated under non-ideal, i.e., in practical situations like at the presence of beam spreads and due to asymmetry of the beam axis with respect to the cavity axis. Though, these two situations arises from the

MIG gun part, but our study is considered only for interaction cavity, considering some possible spread values and misalignment situations, the beam wave interaction studies have been done using CST studio suite.

Velocity spread in the gyrating electron beam is usually present in the electron-beam devices and causes deviations of the beam characteristics and affects device performance [Dumbrajs *et al.*(2013) and Singh *et al.*(2014]. Even though, in present days, the device fabrication and beam launching technologies as well facilities are considerably improved that results a smaller variations in the quality of beam. The amount of velocity spreads and the misalignments are very small but certain amounts are always present in the practical devices. In our study considering velocity spreads of 0%, 5% and 8%, the device performance is analyzed and also evaluated through PIC simulation. Now, for misalignments of beam axis, there is no updated analysis with time dependent multimode theory [Fliflet *et al.* (1991)] and hence, the effects are investigated by simulation CST Studio Suite. The RF power and frequency of oscillations are calculated and tabulated in the Table 3.5 for velocity spreads. It is observed that the velocity spread effects much on the power level but its effect on oscillation frequency deviation is mild.

Table 3.5: RF power and frequencies for different velocity spreads

Velocity spread	RF power (kW)	Frequency (GHz)
0 %	107	94.987
5 %	102.4	94.988
8%	97.8	94.984

With a parallel shift of beam axis from the cavity axis of the interaction structure, in CST Studio suite environment, the design performance has been carried out. The calculated power levels and frequencies of the operating modes are done through PIC simulation. The possibility of beam misalignment happens at the time of

device fabrication and machining the beam source. Since, the complete analysis has been made by assuming the concentric relation between beam and cavity axis geometry. Even though, with the advancements of device machining and fabrication technologies, still there is a mild chance of misalignment can occurs. The effects have been studied in the simulation domain by taking a parallel shift of beam axis from cavity axis with steps, like, d = 0.1 mm, 0.2 mm and 0.3 mm. Similarly, the beam tilt is considered of at most 1^0 in steps of 0.2^0. The RF powers and the oscillation frequency of the device in the TE_{62}- mode at various beam shifts and tilts are simulated and tabulated in Table 3.6 and Table 3.7.

Table 3.6: RF power and frequencies for different beam shifts

Beam shift *d*	**RF power (kW)**	**Frequency (GHz)**
0.1 mm	107	94.987
0.2 mm	101.3	94.985
0.3 mm	96.8	94.984

Table 3.7: RF power and frequencies for different beam tilts

Beam tilt	**RF power (kW)**	**Frequency (GHz)**
0.2^0	101.3	94.973
0.4^0	97.6	94.973
0.6^0	94.7	94.971
0.8^0	94.3	94.97
1.0^0	92.1	94.97

By this, the RF behaviour of interaction cavity designed for 95 GHz, 100kW operating $TE_{6,2}$ mode is studied under ideal beam and various practical conditions . In addition to velocity spreads, accounting misalignment of beam axis with respect to the cavity geometry, the RF behaviour under various modes is done through CST Studio suite. In the high power high frequency RF sources, the ohmic losses generated in the cavity due to metallic nature of walls leads to structural deformation in the cavities

thereby degradation of the system performance. Since, for any RF source the desired characteristics are RF power and its operating frequency. Meanwhile, the microwave devices are majorly dependent on the cavity dimensions, so variations in it causes variations in the RF behaviour and its needs to be e analysed. This leads to study of thermos mechanical effects due to ohmic losses for RF sources are mandatory. In the next section, the calculations of ohmic profile in the gyrotron cavity as well the effect of cavity deformation on the RF performance are discussed in detail. Consequently, a thermal system has been designed by using various extended heat surface elements, i. e., fins. After considering all, the thermo-mechanical behaviour is investigated by using commercial PIC code "COMSOL Multiphysics".

3.6. Thermo-Mechanical Analysis and Optimized Cooling System Design

In gyrotron devices, apart from beam parameters, the RF structure dimension and its material properties also plays crucial role in the RF behaviour of the device. Any changes in structural dimension and material property of the RF interaction cavity not only causes deviation in its oscillation frequency but also degrades the RF output power as well as efficiency of the device apart from additional heating of the device structure. In the beam-wave interaction process, due to the finite electrical conductivity of the cavity walls, some part of the RF waves gets dissipated as the ohmic loss [Edgcombe (1993), and Kartikeyan *et al.* (2013)]. This leads to structure heating which may results in the RF cavity deformations, thereby changes in the oscillation frequency as well as decrease in the RF power output. Hence, an efficient thermal management system needs to be designed and ensured for stable operation of the gyrotron device [Edgcombe (1993), Kartikeyan *et al.* (2013), and Nusinovich *et al.* (2014)]. Thermo-mechanical

studies and its effect on RF behaviour of 1 MW power gyrotrons at 140 GHz, 170 GHz and 240 GHz are investigated using computational fluid domain softwares, like, ANSYS, STAR CCM and COMSOL Multi-physics in [Kumar *et al.* (2012), Liu *et al.* (2018), Q. Liu, Y. Liu, Z. Chen, X. Niu, H. Li, and J. Xu (2018), and Koner *et al.* (2009)] have carried out thermal analysis of RF interaction cavity of a 200kW CW, 42GHz gyrotron using ANSYS code for different coolant flow rate with the axial fins provided on its outer surface. Kumar *et al.* (2012) extended this work for 170 GHz gyrotron with axial as well as radial cooling fins. Q Liu *et al.* (2018) also carried out heat transfer analysis of the RF interaction cavity for the 140 GHz and 240 GHz gyrotrons using ANSYS code and shown the effect of cavity deformations on the multi-mode beam-wave interaction of the device. However, cooling fins and thermal system design and its optimization for the RF cavity of the device is not reported in the published literature accessible with us using COMSOL Multiphysics.

In the present work, the thermal and structural analysis of a tapered cylindrical RF interaction cavity of the gyrotron is carried out. With the help of design relationships, radial cooling fins design on the outer jacket of the middle section of the RF interaction cavity is presented. An optimum thermal system is designed and simulated using "COMSOL Multiphysics" code. Implementation of commercial code "COMSOL Multiphysics" is simpler than those used in previously reported work though equally accurate for this purpose and not explored earlier [Salvi *et al.* (2010)]. For the designed cooling system with different convective heat transfer coefficients, deformations in cavity profile are obtained through this simulation. Nonlinear time-dependent multimode theory is used further to obtain the RF output behaviour of the gyrotrons [Kartikeyan *et al.* (2013), Danly *et al.* (1986), Fliflet *et al.* (1991), and Singh *et al.* (2012)]. An optimum thermal system design thus obtained with maximum possible

deformation in the inner dimension of the RF cavity ensures the gyrotron oscillator RF frequency and power output variations within the specified tolerance limit of the device.

The thermal work is organized as follows: starts with evaluation of the effects of the RF cavity deformations on the resonant frequency of the device, the ohmic loss analysis of tapered interaction cavity that acts as wall load, radial cooling fins design, and role of cooling fins in the heat transfer enhancement and the heat transfer mechanisms of RF structure are presented. The thermo-mechanical analysis simulation set-up without fins and with radial fins using commercial code COMSOL Multiphysics are explained. Later, the simulated results of the RF structure for various convective heat transfer coefficients for different fin groups under optimized values of thermal system parameters are presented followed by its effects on the RF performance of the device due to changed scenario of the electron beam and RF wave interaction are also presented.

3.6.1. Analysis: Calculation of Ohmic Losses and Fin Design

As discussed in Sections 3.1 and 3.2, the RF fields are mainly confined in the middle section of cavity of radius R_c. The heat loading of the cavity walls are differential as per cavity RF field profile. Hence, for stable frequency radiation from gyrotron, we have to provide an efficient cooling system so that its deformation remains minimum so as to keep the oscillation frequency, RF output power and efficiency deviation remains within the tolerance limit of the device.

3.6.1a Effects of radial deformation on resonant frequency

Gyrotron oscillators operate near to cut-off region of its RF interaction cavity. The cavity radius plays a crucial role in governing the radiation frequency of the RF

wave. Using expression (3.1), the dependence of cavity cutoff frequency *fc* with the variations in cavity radius is plotted in Figure 3.14.

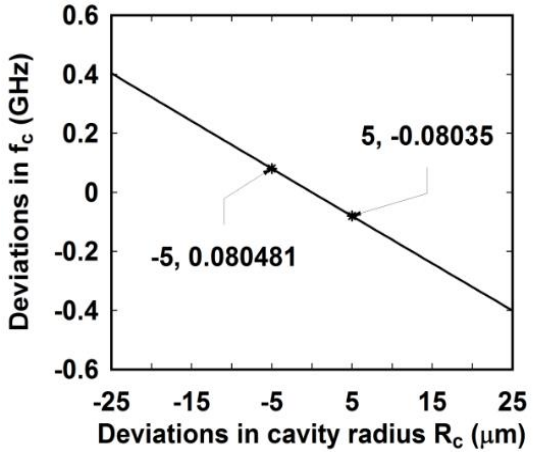

Figure 3.14: Variations in the cavity cut-off frequency fc due to changes in the RF cavity radius R_c.

We can observe from this plot that there is a change in the RF cavity radius, which will result in a significant change in the cavity cutoff frequency thereby will cause significant change in the gyrotrons oscillation frequency. Typically, a 5 μm change in cavity radius results in 80 MHz shift in the device oscillation frequency.

3.6.1.b Wall loss calculation

The Ohmic loss generated in the structure acts as a wall load or heat flux on the structure, and may cause structural deformations. The Ohmic wall losses P_Ω are connected to the Ohmic quality factor Q_Ω of the interaction structure by the well-known relation [Edgcombe (1993)]:

$$P_\Omega = \frac{2\pi f W}{Q_\Omega}, \tag{3.23}$$

with frequency f and stored energy W. A similar expression can be obtained for the diffraction loss P_{diff} as well:

$$P_{diff} = \frac{2\pi fW}{Q_{diff}}. \tag{3.24}$$

Combining equations (3.22) and (3.23), one obtains an expression for the Ohmic loss as a function of the output power $P_{out} = P_{diff}$ as:

$$P_{\Omega} = \frac{P_{diff} Q_{diff}}{Q_{\Omega}}. \tag{3.25}$$

Under the condition of normal skin effect, one gets:

$$P_{\Omega} \approx \frac{Q_{diff}\left(\pi f \mu_o \sigma\right)}{1-\left(m/\chi_{mp}\right)^2} \frac{P_{diff}}{R_c}, \tag{3.26}$$

where, σ is the electrical conductivity of the cavity material, m is the azimuthal mode index and μ_0 is the permeability of free space. Dividing equation (3.25) by the surface area A, gives the power loss density of the middle cavity section as [Nusinovich *et al.* (2014)]:

$$\frac{dP_{loss}}{dA} \approx \sqrt{\frac{1}{30\sigma}} \left(\frac{f^{3/2} P_{out} Q_{diff}}{c^{3/2} L_c} \right) \left(\frac{1}{\chi_{mp}^2 - m^2} \right). \tag{3.27}$$

The above wall load expression (3.26) is for a uniform profile and limited to the middle cavity section of length L_c only. Practically, the power loss density in the cavity is of non-uniform nature and also exists at the up-taper section as well. Thus, the ohmic loss profile along the interaction structure can be written as [Kartikeyan *et al.* (2013)]:

$$\frac{dP_{loss}(z)}{dA} \simeq \left(\frac{\delta}{4\pi\mu_0\omega} \right) \left[\frac{1}{\chi_{mp}^2 - m^2} \right] \left(\frac{\chi_{mp}^4}{R^4(z)} \left| V_{mp} \right|^2 + \frac{m^2}{R^2(z)} \left| \frac{dV_{mp}}{dz} \right|^2 \right). \tag{3.28}$$

Here, m is azimuthal mode index, *R(z)* is the cavity radius at axial position z, V_{mp} is the axial electric field profile of the interaction structure resulted from beam wave interaction analysis and δ is the skin depth. The surface roughness effects of interaction cavity can be accounted by replacing δ with $\delta_{eff} \simeq 2\delta$ [Kartikeyan *et al.* (2013)].

3.6.1c. Cooling Fins Design

For gyrotrons, due to thermal dependency of the materials, efficient heat transfer from the structure is always desired. Generally heat transfer rate can be increased by increasing the temperature gradient between the object and the environment, or by increasing the convection heat transfer coefficient or by increasing the surface area of the object. Here, the concept of increasing the surface area is achieved by incorporating fin surfaces.

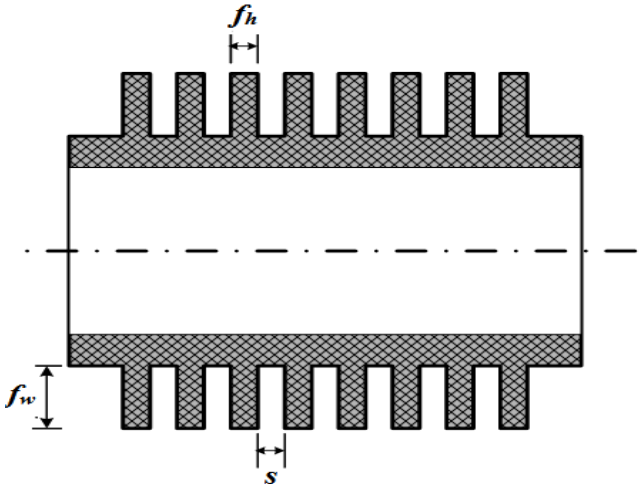

Figure 3.15: Schematic diagram of typical radial cooling fins on a cylindrical surface (f_h = fin height, f_w = fin width and s_f = spacing between fins).

Cooling fins provide an extended surface from the object intended to enhance the heat transfer rate to or from the environment through convection by increasing surface area of the object. In the present study, radial fins type as shown in Figure 3, is considered for the thermal system design.

With radial fins in place, the heat transfer rate q_t, is given by [Incropera *et al.* (2013)]:

$$q_t = hA_t\left[1-\frac{NA_f}{A_t}(1-\eta_f)\right]\theta_b \quad , \tag{3.29}$$

where, h is the convective heat transfer coefficient, A_t is the total surface area associated with the fins and the object, N is the fins number, each fin surface area A_f , single fin efficiency η_f , and θ_b is the temperature gradient between outer surface of the object and environment.

Keeping the goal as less fin area for optimum heat transfer rate; by varying fin geometries, such as, width f_w, height f_h, number of fins N with spacing between fins s_f is achieved, as shown in Figure 3.15.

3.6.1d. Heat Transfer Modes in the RF cavity

Heat transfer, defined as the transmission of thermal energy from one region to another as a result of the temperature gradient. It generally takes place by three different modes: Conduction, convection and radiation. The modes of heat transfer are quantified by the appropriate rate equations which give the heat transfer per unit area.

In the present problem, heat transfer through the conduction and forced convection modes are chosen to analyze the system. For heat transfer by conduction, the rate equation is known as Fourier's law, and the convective heat transfer process is described by the rate equation known as Newton's law of cooling [Incropera *et al.*(2013)]. The heat transfer from the inner surface to the outer surface of the cavity occurs in the conduction mode and from there on by convection mode to the fluid. The effects of the heat transfer on the cavity due to wall loading can be assessed in terms of

surface temperature and radial deformation at the inner and outer walls of the cavity. Heat transfer and structural analyses can be performed using computational fluid domain simulation software, like, ANSYS, STAR-CCM and COMSOL. In the present work, the thermal and structural analysis of the tapered cylindrical RF interaction cavity is carried out adapting a commercial code "COMSOL Multiphysics" whose GUI is more users friendly and simpler to implement than those of ANSYS, used in previously reported work, though is equally accurate [Salvi *et al.* (2010)].

3.6.2. Heat Transfer Analysis Using "COMSOL MULTIPHYSICS"

A commercial code "COMSOL Multiphysics" is adapted here for the structure thermo-mechanical effect investigation. This code is a cross-platform finite element analysis solver and multi-physics simulation software. It allows conventional physics-based user interfaces and coupled systems of partial differential equations. In the present study, the heat transfer module and solid mechanics module in COMSOL is chosen for the thermo-mechanical analysis of the interaction structure.

3.6.2.a COMSOL Multiphysics simulation modeling

In general the investigation process of a problem in COMSOL simulation domain process consists of four steps: 1) modeling of the geometry and assigning materials with given electrical and thermal properties; 2) based on problem investigations, selection of suitable physics modules, assigning the same to the geometry by updating it with the given input conditions, like, type of domain, type of boundaries and initial values, etc.; 3) initializing the study step: by selecting type of study either steady state or time dependent, and coupling between physics modules if necessary; and then 4) Define the mesh distribution by setting sequence type and type of element used for calculations.

In the present problem, considering the symmetry nature of the interaction cavity, for geometry realization 2D axis symmetric model in COMSOL is selected and interaction cavity is modeled as per the parameters listed in Table 3.4. From the material library, the OFHC copper with various material properties at 293.5 K as listed in Table 3.8 are assigned. In the work for both RF and Thermal calculations, the electrical conductivity of the cavity material has been chosen as 5.8e7 S/m. The modeled interaction cavity structures without and with radial fins in the COMSOL Multiphysics are shown in the Figure 3.16.

Table 3.8: Interaction cavity material properties at 293.5 K

Material properties	**Value (units)**
Cavity Material	(OFHC/OF) copper
Density	8939 (kg / m^3)
Electrical conductivity	$5.8*10^7$ S/m
Thermal conductivity	401 (W / (m. K))
Specific heat	383 J / (kg. K)
Elasticity modulus	126 (GPa)
Coefficient of Thermal expansion	$1.6719*10^{-5}$ (1/K)
Poisson ratio	0.3351

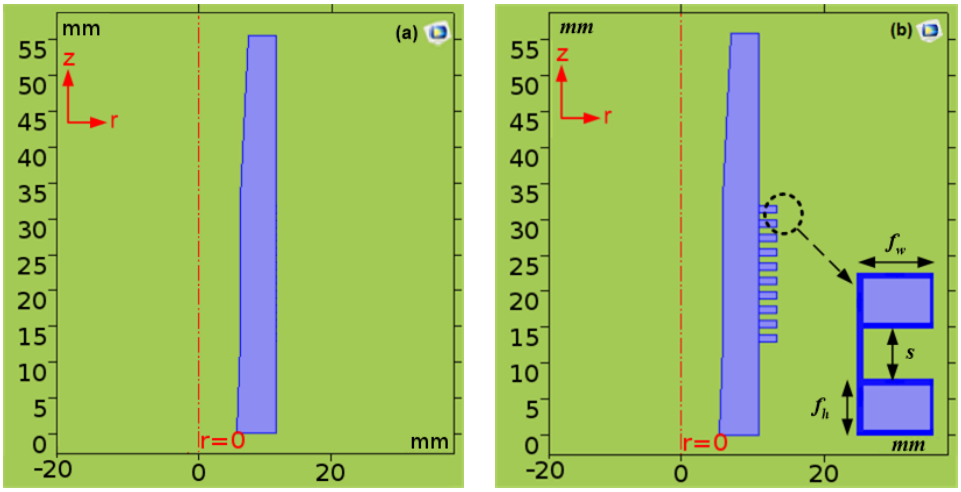

Figure 3.16: 2D axis symmetric interaction cavity models (a) without and (b) with radial fins simulated in COMSOL (fh = fin height, f_w = fin width and s_f = spacing between fins).

Heat transfer in solids and solid mechanics physics modules have been selected for the thermal and structural investigations of the interaction structure respectively and both physics are coupled. Coming to the assigning of boundary conditions, in the heat transfer in solids physics module, the wall loading profile (ohmic power loss density) calculated from expression (3.27) and shown in Figure 3.17, is loaded as the heat flux at the inner wall surface of the structure which causes the thermal effects and leads to structural deformations.

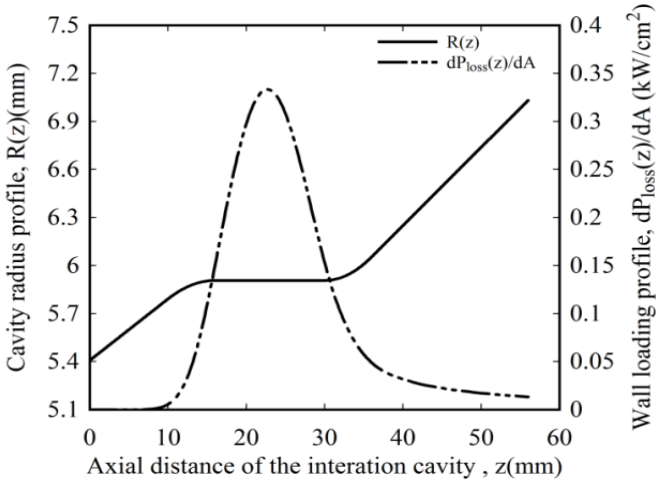

Figure 3.17: Wall loading profile (ohmic power loss density) for operating $TE_{6,2}$ mode of the gyrotron(electrical conductivity σ = 5.8x107 S/m).

Since our goal is to study the thermal effects and thereby designing the optimized cooling system, so the heat flux at the outer cavity walls is chosen in convective heat flux mode that transfers heat from inside to outside surface and thereby restricts the structural deformations, and is explained as:

$$q_o = h(T_{ext} - T_\infty) \quad , \tag{3.29}$$

where T_{ext} is the outer surface temperature of the structure and T_∞ is the ambient temperature. Since, the heat transfer takes from high temperature to low temperature so in the present problem it occurs from inner surface to outer surface that allows surface deformation from inner to outer surface [Incropera *et al.* (2013)]. In the present study, by fixing ambient temperature T_∞ at 293.5 K, for various convective heat transfer coefficient h (W/m^2.K) values the simulations are carried out. The axial end surfaces of the interaction cavity not subjected to heat flux are thermally insulated for the study.

The temperature distribution of the interaction cavity resulted from the heat transfer in solids physics module is coupled to the solid mechanics physics module as thermal load for the deformations study. Maintained fixed constraints on the axial end surfaces and free to move constraints on the radial surfaces of the interaction cavity, the structural deformations have been calculated. A steady-state, with coupling between physics modules study and sequence type of physics controlled mesh with extremely fine element type is selected for the simulations.

Firstly, the thermo-mechanical analysis using COMSOL Multiphysics code is performed by considering various thickness values of the interaction cavity from the middle section, δR = 3 mm to 7 mm at different values of heat transfer coefficient h of the coolant under no fins condition. Then, by considering radial fins over the middle section with various fin width $f_{w,}$ fin height f_h, spacing between fins s, and different number of fins N, the thermo-mechanical analyses on interaction cavity are also carried out.

In the present work, considering radial fins along the middle section of the cavity (L_c), the thermal system is optimized by maintain the temperature of coolant at room temperature. The allowed tolerances of radial deformations (increase) at the inner

cavity radius is upto 6 μm such that oscillation frequency shifts at maximum upto 0.1 GHz [Kartikeyan *et al.* (2013)] with average outer surface cavity temperature ~ 300 K. For this purpose, different convective heat transfer coefficient *h* values are chosen which solely describe the fluid dynamics parameters [Incropera *et al.* (2013)], such as, fluid flow rates, hydraulic diameter, etc. Generally, in forced convection mode, for liquids, heat transfer coefficient *h* lies in the range between 100-20000 ($W/m^2.K$) and for convection with phase change boiling or condensation; the heat transfer coefficient *h* lies in the range of 2500-100000 ($W/m^2.K$) [Incropera *et al.* (2013)]. In the present problem, the study is limited with heat transfer coefficient *h* from 4000 to 20000 ($W/m^2.K$), means no boiling or condensation of the fluid in the cooling system design is allowed.

The impact of thermal system parameters on the RF interaction cavity under the ohmic wall loss are assessed in terms of cavity outer surface temperatures by thermal analysis and radial deformations at cavity inner surfaces by structural analysis and are discussed in detail. Subsequently, the thermo-mechanical effects on the RF behaviour of the interaction cavity at optimized cooling system parameters are investigated using the nonlinear time-dependent multimode theory [Fliflet *et al.* (1991)].

3.6.3 Result and Discussion

The thermo-mechanical effect of ohmic loss generated due to the microwave power radiated in the tapered cylindrical interaction cavity of the gyrotron has got investigated. The structure is modeled and simulated using commercial code "COMSOL Multiphysics". Considering various cavity thickness δR values at different convective heat transfer coefficient *h* values, for without fins and with radial fins groups are studied. Initially, investigations are carried out for structure without fins, labeled as

"WOG" group. As described in above, the effects are measured in terms of radial deformations (increase) ΔR_{rad} at inner and temperatures T_{out} at outer surface of the interaction cavity.

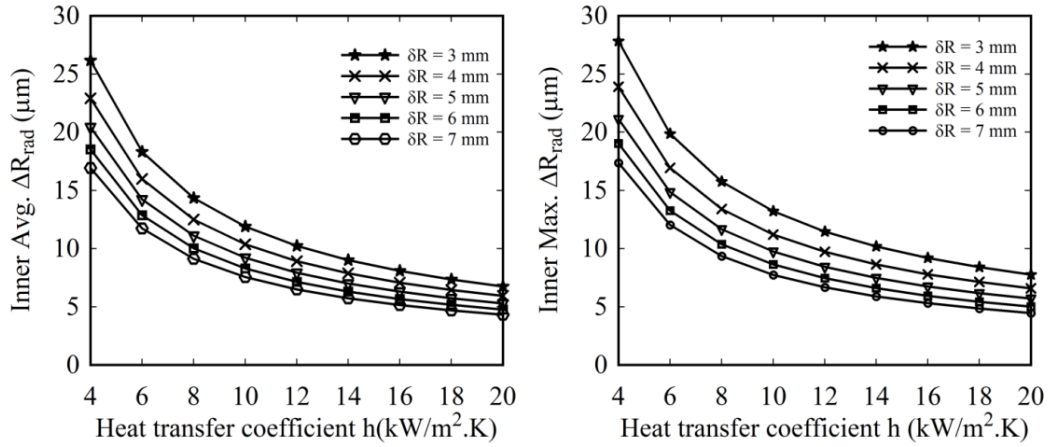

Figure 3.18: Radial deformation ΔR_{rad} at the cavity inner surface for various heat transfer coefficient h and cavity thickness δR values (a). Average and (b) Maximum.

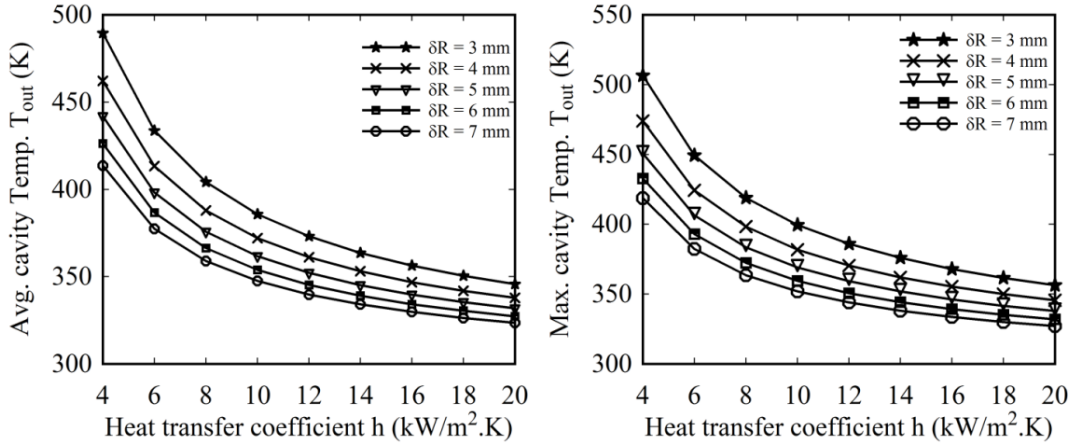

Figure 3.19: Temperature at the cavity outer surface Tout for various heat transfer coefficient h and cavity thickness δR values (a) Average and (b) Maximum.

Since, due to the non-uniform nature of the heat flux, for the initial study, both the average and maximum values of inner ΔR_{rad} and T_{out} at inner and outer surfaces are plotted as Figures 3.18 -3.19, respectively.

As expected, it can be easily observed from the Figures 3.19-3.20 that for higher values of convective heat transfer coefficient *h*, the amount of radial deformations (increase) and the temperature values of the cavity are decreasing monotonically with increasing of cavity thickness δR means increment in the heat transfer rate. In order to restrict the magnitudes of radial deformations (increase) ΔR_{rad} and the cavity temperatures T_{out} under the desired values, radial type fins have been introduced on the outer surface of the interaction cavity. From the preliminary studies without fins (WOG group), the probable range of convective heat transfer coefficient *h* and cavity thickness δR are suitable for the optimum thermal system design of cavity structure are selected. Secondly, there is a nominal variation in the average and maximum levels of radial deformations ΔR_{rad} at the inner surface, as well as considering the temperatures at the outer surface the average surface T_{out} are of important for the optimization of the thermal design. Thus, the variations of maximum inner radial deformations (increase) ΔR_{rad} and average outer surface temperatures T_{out} for the fin groups are shown in the rest of the analysis.

For achieving the desired performance of the thermal system with minimum fins area is always desired and, the fins area is increased by varying the fins geometrical parameters in a systematic way and simultaneously observing the maximum radial deformations (increase) and average temperature values of the interaction cavity by using COMSOL Multiphysics. Considering moderate power levels in the interaction cavity, the radial fin groups labeled as RG1, RG2, RG3, and RG4 are placed in the middle part region (L_c) on the outer surface of the RF interaction cavity. Different geometrical parameters of the fin groups are listed in Table 3.9 with uniform spacing s = 1 mm between the fins.

Table 3.9: Dimension of various radial fin groups

Fin group	Fin width f_w (mm)	Fin height f_h (mm)	Number of fins N
WOG	0	0	0
RG1	2	1	10
RG2	2.5	1	10
RG3	3	1	10
RG4	3.5	1	10

The thermo-mechanical simulations are carried out with the various fins groups for the range of convective heat transfer coefficient h from 8000 to 16000 (W/m^2.K), and cavity thickness δR=3 mm to 5 mm. Maximum inner radial deformation (increase) ΔR_{rad} and average cavity outer surface temperatures T_{out} for the fin groups are tabulated in Table 3.10 and Table 3.11.

Table 3.10: Maximum values of radial deformations (increase) ΔR_{rad} at cavity inner surface for various radial fin groups (RG1, RG2, RG3, RG4) at various heat transfer coefficient h and thickness δR values.

Heat transfer coefficient, h (W/m^2.K)	δR, mm	WOG ΔR_{rad} (µm)	RG1 ΔR_{rad} (µm)	RG2 ΔR_{rad} (µm)	RG3 ΔR_{rad} (µm)	RG4 ΔR_{rad} (µm)
8000	3	15.752	6.920	6.070	5.424	4.907
8000	4	13.384	6.186	5.084	4.554	4.135
8000	5	11.672	5.608	4.416	3.967	3.614
10000	3	13.211	5.774	5.474	4.921	4.483
10000	4	11.205	5.164	4.584	4.137	3.782
10000	5	9.742	4.682	3.986	3.609	3.311
12000	3	11.465	5.000	5.011	4.582	4.297
12000	4	9.717	4.476	4.200	3.853	3.625
12000	5	8.433	4.061	3.657	3.365	3.174
14000	3	10.182	4.441	4.807	4.405	4.151
14000	4	8.629	3.980	4.010	3.716	3.521
14000	5	7.479	3.614	3.484	3.254	3.097
16000	3	9.193	4.016	4.653	4.248	4.016
16000	4	7.794	3.605	3.900	3.599	3.421

16000	5	6.751	3.277	3.402	3.163	3.020

Table 3.11: Average cavity outer surface temperatures of various radial fin groups (RG1, RG2, RG3, RG4) at various convective heat transfer coefficient *h* and cavity thickness δR values.

Heat transfer coefficient *h* (W/m2.K)	***δR* mm**	**WOG T_{out} (K)**	**RG1 T_{out} (K)**	**RG2 T_{out} (K)**	**RG3 T_{out} (K)**	**RG4 T_{out} (K)**
8000	3	404.2	339.9	333.3	328.1	323.9
8000	4	387.8	334.4	328.8	324.3	320.6
8000	5	375.7	330.1	325.1	321.2	318.0
10000	3	385.8	331.0	325.5	321.2	317.8
10000	4	372.0	326.5	321.8	318.1	315.2
10000	5	361.7	323.0	318.9	315.6	313.0
12000	3	373.0	325.0	320.3	316.7	313.8
12000	4	361.1	321.2	317.2	314.0	311.5
12000	5	352.2	318.2	314.7	311.9	309.7
14000	3	363.6	320.6	316.5	313.4	310.8
14000	4	353.0	317.3	313.8	311.1	308.9
14000	5	345.1	314.7	311.7	309.3	307.3
16000	3	356.3	317.3	313.7	310.9	308.7
16000	4	346.8	314.4	311.3	308.9	307.0
16000	5	339.7	312.1	309.4	307.3	305.6

For the radial fin groups RG3 and RG4, the range of *h* from 14000 to 16000 with δR = 5 mm, the maximum inner radial increase is less than 3.25 μm which is of our design constraint and the average cavity outer surface temperature is at 310 K.

For the optimum range of heat transfer coefficient *h* values, considering water as a coolant with T_{fluid} at 293.15 *K*, the range of various thermal system parameters, like, hydraulic diameters (D_h) through which the coolant is flown, at different water flow rates are calculated and are shown in the Figure 3.20 [Incropera *et al.* (2013)].

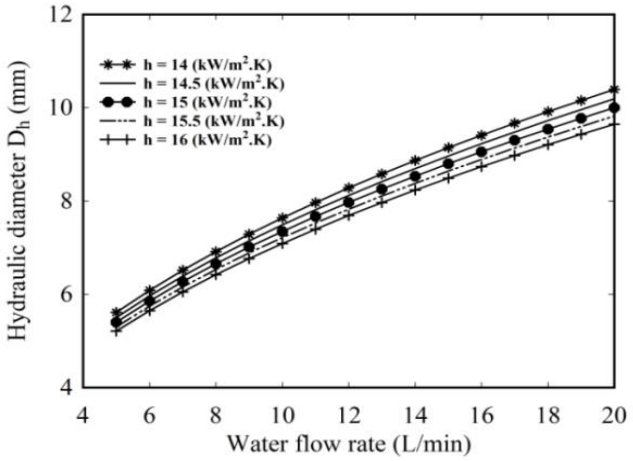

Figure 3.20: Range of hydraulic diameter D_h and water flow rates of the thermal system for the optimized convective heat transfer coefficient h values.

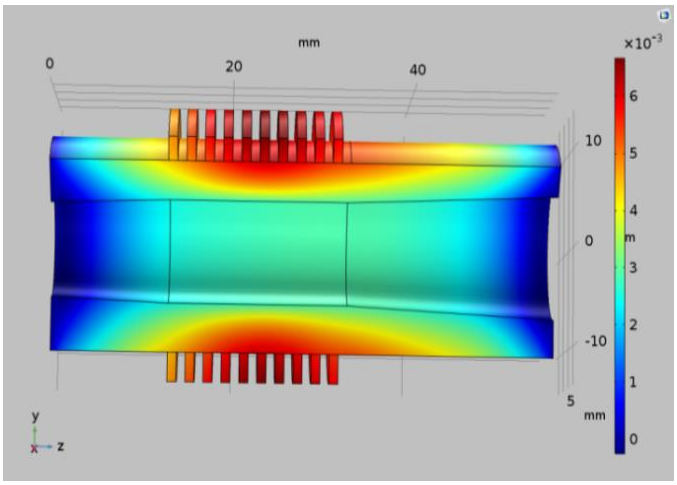

Figure 3.21: 3D view of the radial deformation distribution for heat transfer coefficient h=15000 (W/m2.K) and δR=5 mm of RG3 group.

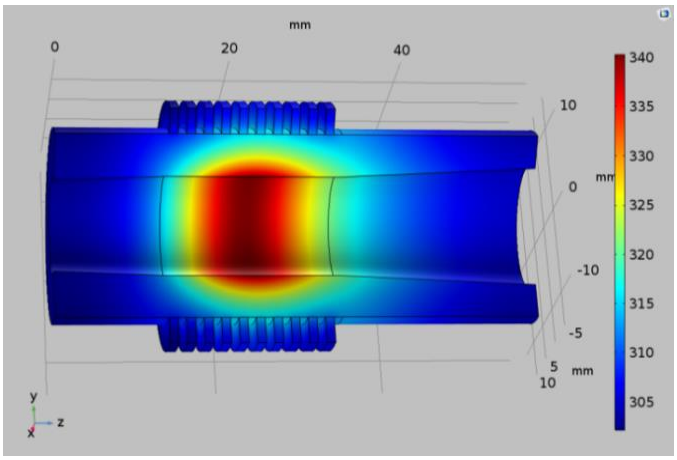

Figure 3.22: 3D view of temperature distribution for heat transfer coefficient h=15000 (W/m2.K) and cavity δR= 5 mm of RG3 group.

The 3D view of temperature distribution and the radial deformation (increase) distribution of interaction cavity for optimized heat transfer coefficient h as 15000 ($W/m^2.K$) and cavity thickness δR = 5 mm, for RG3 fins group, are shown in Figures 3.21 and 3.22.

It can be observed that the average value of cavity outer surface temperature T_{out} is around $308K$ and the maximum radial increase ΔR_{rad} at the inner surface of the cavity is ~3.2µm that is within tolerable limits of the targeted design parameters. The deformations occurring around the outer surface is of maximum 6 µm, a collective one from inner to outer surface. Comparatively, the surface deformation at the inner walls is more because of the presence of heat source which causes larger temperature rise than the coolant temperature. Due to the coolant, the heat transfers faster to the outer surface thereby maintaining desired operation. The cavity radius profiles of initial and the deformed cavity with in tolerable limits at the optimized cooling system parameters are shown in Figure 3.23.

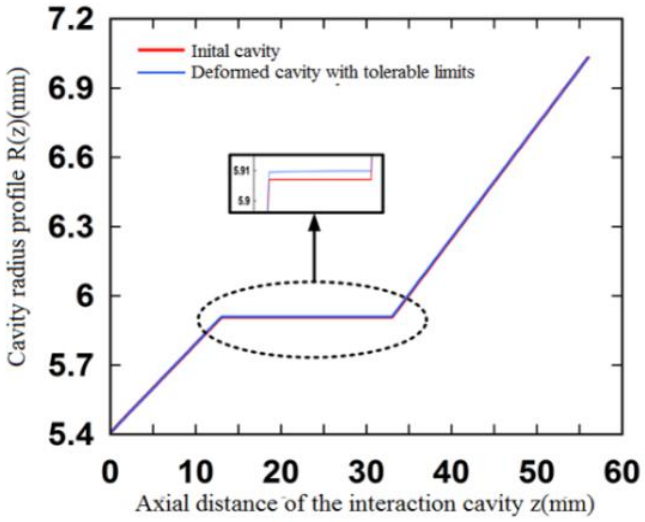

Figure 3.23: Initial (red colour) and deformed cavity (blue colour) due to ohmic loss at optimized thermal system parameters.

Now, the study is further extended to investigate thermo-mechanical effects on the RF behaviour of the deformed cavity with tolerable limits at initial and final (steady state) conditions. RF behaviour of the device under both conditions, cold (in absence of electron beam) as well as hot (in presence of electron beam) are investigated. At cold condition, the axial RF field profile and the resonant frequency and quality factors of the cavity are calculated by solving the wave equation in the cavity at radiation boundary conditions that leads minimum reflection mentioned in Section 3.2. The comparisons of cavity field amplitudes with resonance frequency and quality factors of both initial and deformed conditions (with RG3 fins, h =15000 W/m^2.K, δR = 5 mm) are plotted in Figure 3.24. It can be observed that with designed cooling system, maximum reduction in the resonant frequency f_{res} is 48 MHz and a decrement of 20 in the diffractive quality factor Q_{diff} occurred from the initial cavity values (cold condition).

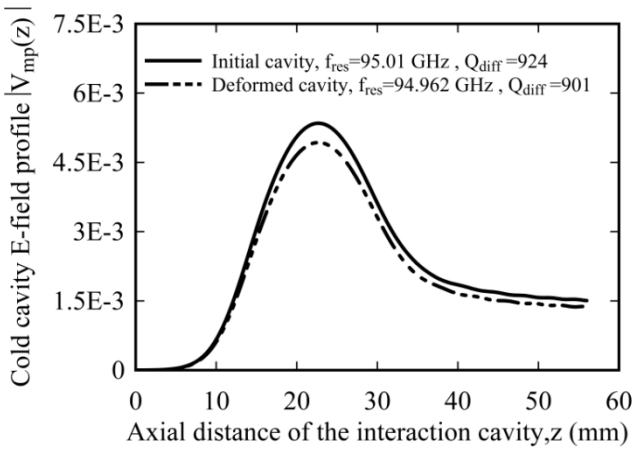

Figure 3.24: Cold cavity field amplitude profiles for the initial and deformed cavity.

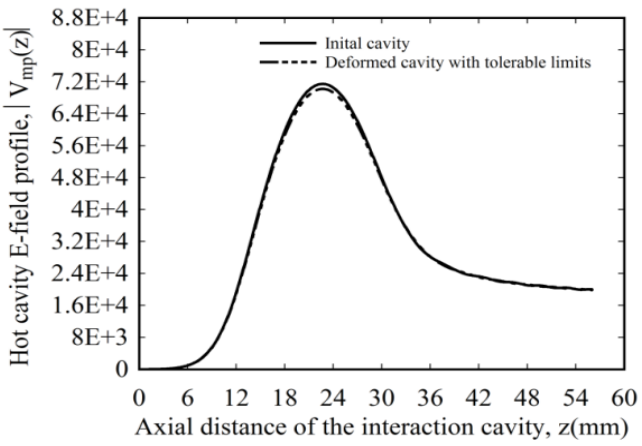

Figure 3.25: Hot cavity electric field profiles of initial and deformed cavity.

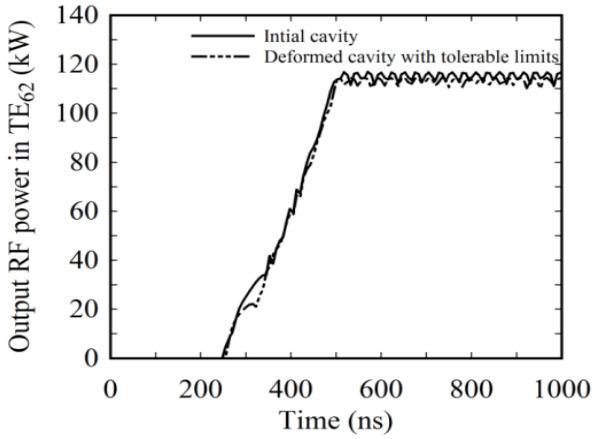

Figure 3.26: Comparisons of power levels in the $TE_{6,2}$ for initial and deformed cavity.

To study the effect of cavity deformation under hot (in presence of electron beam) condition, we have revisited the non-linear, time dependent, multimode theory of the gyrotrons presented in Section 3.5. Maintaining the same beam parameters with zero velocity spread, gyrotron device performance with the deformed RF interaction cavity is obtained. The field amplitude profile and power levels in various modes are calculated. Comparisons of hot cavity field amplitude profiles and the output power levels in the operating modes $TE_{6,2}$ for initial and deformed cavity with tolerable limits are plotted in Figures 3.25 and 3.26. It can easily be noted a reduction of ~ 2 kW in RF output power in the case for the deformed cavity from the initial cavity gyrotron device.

3.7. Conclusions

In the present chapter, the design, analysis and PIC simulations of RF interaction cavity of gyrotron operating $TE_{6,2}$ mode at 95GHZ for generation of 100kW of RF power has been presented. Considering the velocity spreads and misalignments of the beam axis with respect to the cavity axis, the structures have been simulated in the Commercial "CST studio suite". In addition, the effect of ohmic losses due to RF generation has been evaluated by the thermal studies with the help of a commercial PIC tool "COMSOL Multiphysics". It is observed that, the beam axis shift and tilt are affecting majority on RF power level and mildly on the operating frequency. Secondly, for small transverse dimensions structures, the thermal losses are significant and needs an efficient cooling system for longer life and reliable operation. Though, $TE_{6,2}$ is one of suitable mode in the 95GHz regime for gyrotrons, but observing the effects of misalignments and thermal losses on the frequency of operation, the interest has been raised to see the use of volumetric modes as the operating mode and its effects on the RF performance and thermal studies under some practical considerations like beam shift. Beam tilt and velocity spreads.

After the beam-wave interaction behaviour study of the gyrotron, the thermo-mechanical study of the RF interaction cavity, its effects on the RF power generation have been carried out for a $TE_{6,2}$, 95 GHz, 100 kW gyrotron. Thermal system design has been validated using a commercial PIC tool, which was not found in the published literature to the authors, using "COMSOL Multiphysics" commercial tool. Implementation of this code has been found simpler than those previously reported though equally accurate. For stable device operation, with the help of the design relationships, radial cooling fins design for the cavity has been presented. Further, describing the approach, an optimum thermal system has been designed and

performance got simulated. Thermo-mechanical behaviour of the interaction cavity structure for various cavity thicknesses, and convective heat transfer coefficient values under without fins and with radial fins conditions have also been investigated. Considering water as coolant at room temperature ~293 K, the range of hydraulic diameter and flow rates have been determined for the optimum convective heat transfer coefficient values from 14000 - 16000 W/m2.K. An optimized simple cooling system thus designed keeps the maximum RF cavity radius deformation (increase) ~ 3.2 μm maintaining the average cavity outer surface temperature of 308 K. Furthermore, a nonlinear time-dependent multimode analysis has also been carried out to observe the RF output behaviour of the gyrotron under such condition. A decrease in its resonance frequency of 48 MHz and a decrement of 20 in the diffractive quality factor of the RF interaction cavity with the reduction of 2 kW of RF output power have been observed in the case for the deformed cavity from those of the initial cavity gyrotron device, which are within the tolerance limit of such devices. We hope that the thermo-mechanical analysis, radial cooling fins and cooling system design, its optimization as well as description of simpler simulation technique using commercial code "COMSOL Multiphysics" for the gyrotron RF interaction cavity carried out here would be useful not only to the tube designers but also to the high power microwave system developers.

Keeping above mentioned points for the gyrotron in our mind and in order to mitigate the thermo-mechanical issues; in the upcoming Chapter, Chapter 4, the same rating gyrotron device operating at a relatively high order mode will be investigated. As we know that the RF structure of the device operating at the higher order mode will be larger. Hence it is expected that here thermo-mechanical issues will get relaxed. Such gyrotron device design, its RF analysis that includes nonlinear section including thermo-mechanical analysis will be carried out and presented in Chapter 4.